Ballistic miniband conduction in a graphene superlattice

Menyoung Lee,[1] John R. Wallbank,[2] Patrick Gallagher,[1] Kenji Watanabe,[3]
Takashi Taniguchi,[3] Vladimir I. Fal'ko,[2,4] and David Goldhaber-Gordon[1*]

[1]Department of Physics and Geballe Laboratory for Advanced Materials,
Stanford University, Stanford, California 94305, USA

[2]National Graphene Institute, University of Manchester, Booth St. E, Manchester, M13 9PL, UK

[3]National Institute for Materials Science, 1-1 Namiki, Tsukuba 305-0044, Japan

[4]School of Physics & Astronomy, University of Manchester, Oxford Road, Manchester, M13 9PL, UK

[*]To whom correspondence should be addressed; e-mail: `goldhaber-gordon@stanford.edu`

Abstract

Rational design of long-period artificial lattices yields effects unavailable in simple solids. The moiré pattern in highly aligned graphene/h-BN heterostructures is a lateral superlattice with high electron mobility and an unusual electronic dispersion whose miniband edges and saddle points can be reached by electrostatic gating. Here we investigate the dynamics of electrons in moiré minibands by measuring transverse electron focusing—ballistic transport between adjacent local contacts in a magnetic field. At low temperatures, we observe caustics of skipping orbits extending over hundreds of superlattice periods, reversals of the cyclotron revolution for successive minibands, and breakdown of cyclotron motion near van Hove singularities. At high temperatures, electron-electron collisions suppress focusing. Probing such miniband conduction properties is a necessity for engineering novel transport behaviors in superlattice devices.

In solids, the quantum nature of electrons generates band structure, which controls conduction and optical properties. Similarly, longer-period superlattices generate minibands that disperse at a finer energy scale over a reduced Brillouin zone, enabling phenomena such as negative differential conductance and Bloch oscillations [1–3]. However, fabricating long-range periodic patterns that strongly modulate the potential to form well-separated minibands without undermining the material quality and electron coherence remains challenging. Most experiments on laterally patterned semiconductor heterostructures have revealed classical commensurability effects [4–6], which do not require well-formed and separated minibands. Despite evidence for Fermi surface reconstruction in a patterned superlattice, details of Fermi surfaces were obscured by poor separation between minibands and consequent magnetic breakdown across weakly avoided crossings [7].

The arrival of high-quality van der Waals heterostructures of graphene and hexagonal boron nitride (h-BN) with misalignment angle below 1° [8, 9] has drastically changed the situation. In

such systems, the periodic potential for electrons in graphene is imposed by the hexagonal moiré pattern generated by the incommensurability and misalignment between the two crystals [10–12]. Formation of minibands for Dirac electrons has been demonstrated by scanning tunneling [13], capacitance [14], and optical [15] spectroscopies, as well as magnetotransport [16–19]. These studies have elucidated the electronic structure known as the Hofstadter butterfly which emerges in quantizing magnetic field [20]. By contrast, a small magnetic field may be treated semiclassically. Then the connection between the miniband dispersion $\varepsilon(\vec{k})$ and transport properties is established by the equations of motion for an electron in an out-of-plane magnetic field $\vec{B} = B\hat{z}$,

$$\hbar\vec{v} = \frac{\partial \varepsilon}{\partial \vec{k}}, \quad \hbar\dot{\vec{k}} = -e\vec{E} + eB\hat{z}\times\vec{v}, \tag{1}$$

where the relation between carrier velocity $\vec{v}$ and momentum $\hbar\vec{k}$ is approximately $\vec{v} = v\vec{k}/k$ ($v \approx 10^6$ m/s) close to the Dirac point of graphene's spectrum [10, 11, 13, 14].

The shape of the cyclotron orbit in a 2D metal is a 90° rotation of the shape of the Fermi surface, and the carrier revolves along it clockwise or counterclockwise. Electron trajectories near the boundary of a metal open into skipping orbits [21], which drift in the direction determined by the effective charge of the carrier. These skipping orbits bunch along caustics [22–27], leading to the transverse electron focusing (TEF) effect [22, 23]. Experimentally, TEF takes place when the magnetic field is tuned such that caustics of skipping orbits, emanating from an emitter E, end up at a collector C, located at position $x = L$ along the boundary. Then a voltage V_C is induced at C, proportional to the current I_E injected into E. Figure 1B illustrates skipping orbits and caustics in a material with an isotropic Fermi surface, such as unperturbed graphene near the Dirac point, where TEF occurs for $B = B_j \equiv \frac{2j\hbar k_F}{\pm eL}$ (for $j = 1, 2, ...$). An equidistant series of peaks (oscillations) appears in the focusing "spectrum"—the non-local magnetoresistance $V_C/I_E(B)$ (Fig. 1C), from which the Fermi momentum $\hbar k_F$ and the sign of effective charge $\pm e$ may be inferred. TEF was initially used to study the Fermi surfaces of bulk metals [22, 28], and was later extended to 2D systems [23], including graphene [29].

Here we report the observation of TEF in a moiré superlattice at the interface between graphene and h-BN in a van der Waals heterostructure (from top to bottom) h-BN/graphene/h-BN/bilayer graphene assembled on an SiO$_2$ substrate. One of the h-BN layers (we do not know which) is aligned with graphene to better than 1°, forming a moiré pattern with a 14 nm period [30]. We use the bilayer graphene as an electrostatic gate, tuning electron density in the superlattice by applying voltage V_g to it. The device (Fig. 1A) has three etched local contacts along the linear sample boundary. Two other ohmic contacts are grounded and act as absorbers. We measure the multi-terminal, non-local resistance $(V_M - V_R)/I_L$ at our base temperature $T = T_{base} = 1.55$ K. Figure 2B is the resulting map of $(V_M - V_R)/I_L$ as a function of B and V_g, exhibiting electron focusing spectra and their evolution as a function of electron density n. When the Fermi level in graphene is close to the Dirac point at $V_g = -0.4$ V, the superlattice spectrum is almost isotropic, and $k_F = \sqrt{\pi|n|}$. Hence the focusing spectra show TEF oscillations with peaks at $B_j = \frac{2j\hbar}{\pm eL}\sqrt{\pi|n|}$ (dashed curves in Fig. 2B) as in unperturbed graphene [29]. The observation of TEF confirms that electrons travel ballistically from emitter to collector. The visibility of up to 8 focusing peaks (Figs. 1C, 2B) shows that carrier reflection at the boundary is mostly specular: each peak is lower than the last by a factor of the probability of diffuse scattering [22]. Quantum effects are suppressed because the thermal length $\frac{\hbar v_F}{kT}$ is shorter than the emitter-collector separation L.
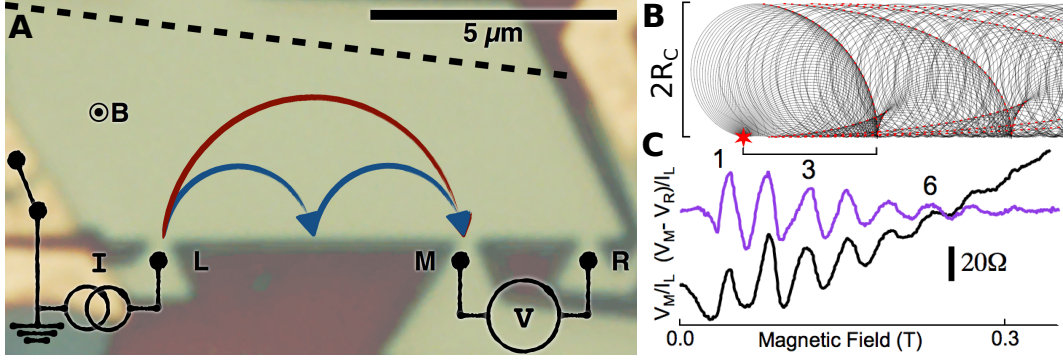
Fig. 1. Experimental concept. (**A**) Schematic of the experiment overlaid on a photo of the device. The h-BN/graphene/h-BN/bilayer graphene heterostructure is green, the SiO_2 substrate is purple, and the dashed line denotes the upper boundary of the graphene flake. Electrical measurement configuration applied to obtain data in Fig. 2B: the two leftmost contacts are grounded to act as absorbers. We inject current into the left local contact L and measure the voltage difference between two local contacts, M and R. Arrows depict skipping orbits a hole would take if injected at normal incidence with $B = B_1 \equiv \frac{2\hbar k_F}{eL}$ (red) or $B_2 \equiv \frac{4\hbar k_F}{eL}$ (blue). (**B**) Ensemble of simulated skipping orbits emanating from an emitter (red star). Electron trajectories bunch along caustics (red dashed curves) and focus onto an equidistant array of points at the boundary. Scale markers show the cyclotron diameter $2R_C = \frac{2\hbar k_F}{eB}$. (**C**) Transverse electron focusing (TEF) spectra collected at a single voltage probe M ($V_M/I_L(B)$, lower trace), and differentially between voltage probes M and R (($V_M - V_R$)/$I_L(B)$, upper trace), with $n = -1.1 \times 10^{12}$ cm^{-2} and $T = 1.55$ K. The first, third, and sixth focusing peaks are labeled. Taking the differential measurement of the spectrum does not shift peak positions, because the device geometry partially shields R from being reached by skipping orbits from L, such that oscillations of V_R are much weaker.

At higher densities approaching four electrons (or holes) per moiré unit cell, the Fermi level is near the first minibands' outer edges, and TEF spectra reflect the modification of electronic states by the superlattice potential. A candidate miniband structure from the model family proposed in [12] is rendered in Fig. 2A, where we label relevant minibands. Carrier dynamics in the form of skipping orbits and caustics are represented using ensembles of simulated electron trajectories in Fig. 3. The map of measured TEF spectra, Fig. 2B, matches the theoretically simulated spectra, Fig. 2C, obtained by applying Eq. (1) to the electrons emitted into the minibands of Fig. 2A from a local emitter at the sample edge [30].

Most interestingly, in addition to TEF of electrons in C1 and holes in V1, both theory and experiment show focusing of holes in C2 and electrons in V2: carrier charge is reversed compared to the corresponding (conduction or valence) band of graphene. For $V_g > V_c^3$, where V_c^3 is the lower band edge of C3, the electron-like pocket of C3 overlaps in energy with the hole-like pocket of C2, leading to TEF oscillations for both signs of B. TEF oscillations abruptly terminate at gate voltage values V_v^1, V_c^1, V_v^2, and V_c^2, which coincide with the passing of the Fermi level across the saddle point van Hove singularities (VHS) at which the constant energy contour of the miniband dispersion percolates across all repeated Brillouin minizones. At these saddle points, cyclotron orbits experience an extreme variant of magnetic breakdown termed orbital switching [31]—opening up into run-away trajectories such that electrons do not drift along the edge of the sample following skipping orbits. In the ranges $V_v^2 < V_g < V_v^1$ and $V_c^1 < V_g < V_c^2$, the Fermi surface consists of small and highly anisotropic pockets just above or below the secondary Dirac points. Thus even the theoretically calculated pattern in Fig. 2C is both weak and dense—experimental observation of these pockets
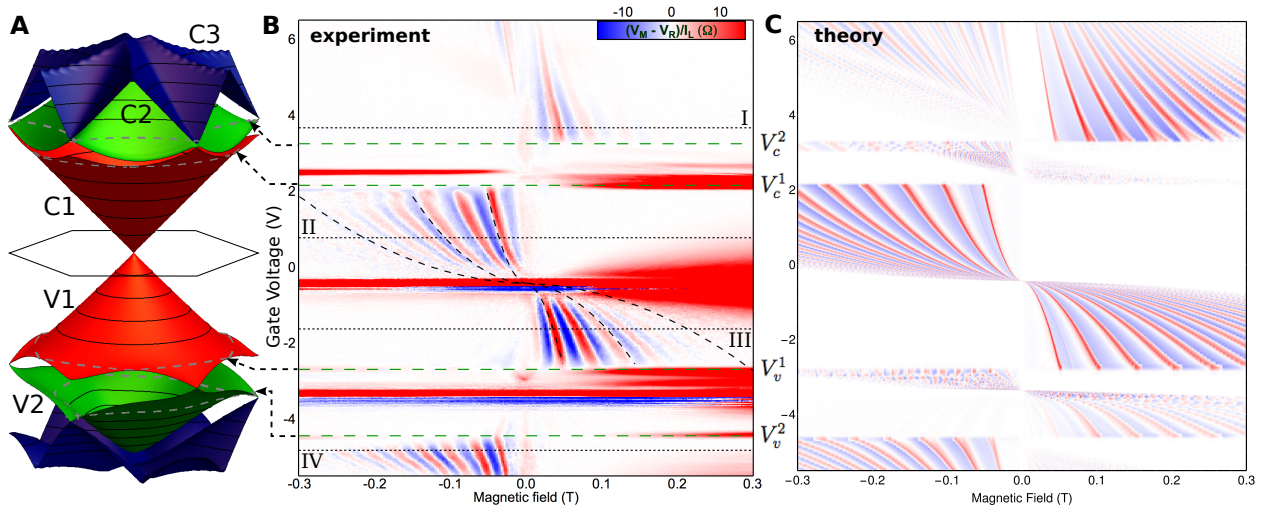
Fig. 2. TEF spectra at base temperature. (**A**) Miniband structure of the graphene/h-BN superlattice, calculated as in [12, 30]. Each miniband for which we observe TEF is labeled as shown. This dispersion results from a symmetric moiré perturbation: $\epsilon^+ = 17$ meV and $\epsilon^- = 0$ meV; this choice gives the best match between experiment (B) and theory (C) [30]. Equipotential contours are shown; the dashed contours are at the energy levels of saddle point VHS. (**B**) TEF spectra as a function of gate voltage V_g. $T = 1.55$ K. The plotted ratio $(V_M - V_R)/I_L$ is measured as depicted in Fig. 1A. Black dashed curves: B_1, B_3, and B_6, which are some of the peak positions expected when the Fermi level is close to the Dirac point. Green dashed lines indicate the abrupt termination of TEF caused by the breakdown of cyclotron motion at each VHS. Dashed arrows to (A) point to the energy levels (dashed contours) of the corresponding VHS, and voltage values are labeled by the miniband in which the breakdown occurs, e.g. V_c^1 for the breakdown of cyclotron motion in C1. Dotted lines: selected densities, I, II, III, and IV, which place the Fermi level in minibands C2, C1, V1, and V2, respectively. (**C**) TEF spectra as a function of V_g, calculated from the dispersion in (A) and Eq. (1) [30].

is obscured because of smearing by finite emitter and collector widths and suppression by partial diffusivity of reflection from the edge.

The positions of saddle points, $V_v^1, V_c^1, V_v^2,$ and V_c^2, can be directly compared to miniband models. We tested the observed ratios $\frac{V_v^1 - V_v^2}{V_c^1 - V_v^1}$ and $\frac{V_c^2 - V_c^1}{V_c^1 - V_v^1}$ against predictions from a family of moiré superlattice models parameterized by strengths of inversion-symmetric (ϵ^+) and antisymmetric (ϵ^-) interlayer coupling between graphene carbons and the boron and nitrogen sites of h-BN [30, 32]. The best match to experimental data corresponds to an inversion-symmetric moiré perturbation with $\epsilon^+ \approx 17$ meV, $\epsilon^- \approx 0$ (Fig. S2), which we used to calculate the miniband structure, electron dynamics, and TEF maps in Figs. 2 and 3. This value for ϵ^+ is similar to previous estimates from optical spectroscopy [15].

We can learn more about carrier dynamics, in particular the effect of their scattering, by examining the temperature dependence of TEF oscillations [28]. Throughout the probed temperatures and densities, the suppression of TEF upon heating (Fig. 4A) is faster than what could be expected from merely thermal broadening of injected electron momenta, as $|k - k_F| \sim \frac{k_B T}{\hbar v_F} \ll k_F$. For quantitative analysis, we determine the area A_1 under the first ($j = 1$) focusing peak and interpret the ratio $A_1(T)/A_1(T_{base})$ as the fraction of electrons $e^{-\pi L/2v_F\tau}$ that propagated ballistically from the emitter to the collector, along the semicircular cyclotron trajectory of length $\frac{\pi L}{2}$ that touches the caustic near the collector, despite the electrons scattering with a characteristic rate τ^{-1}. Figure 4B
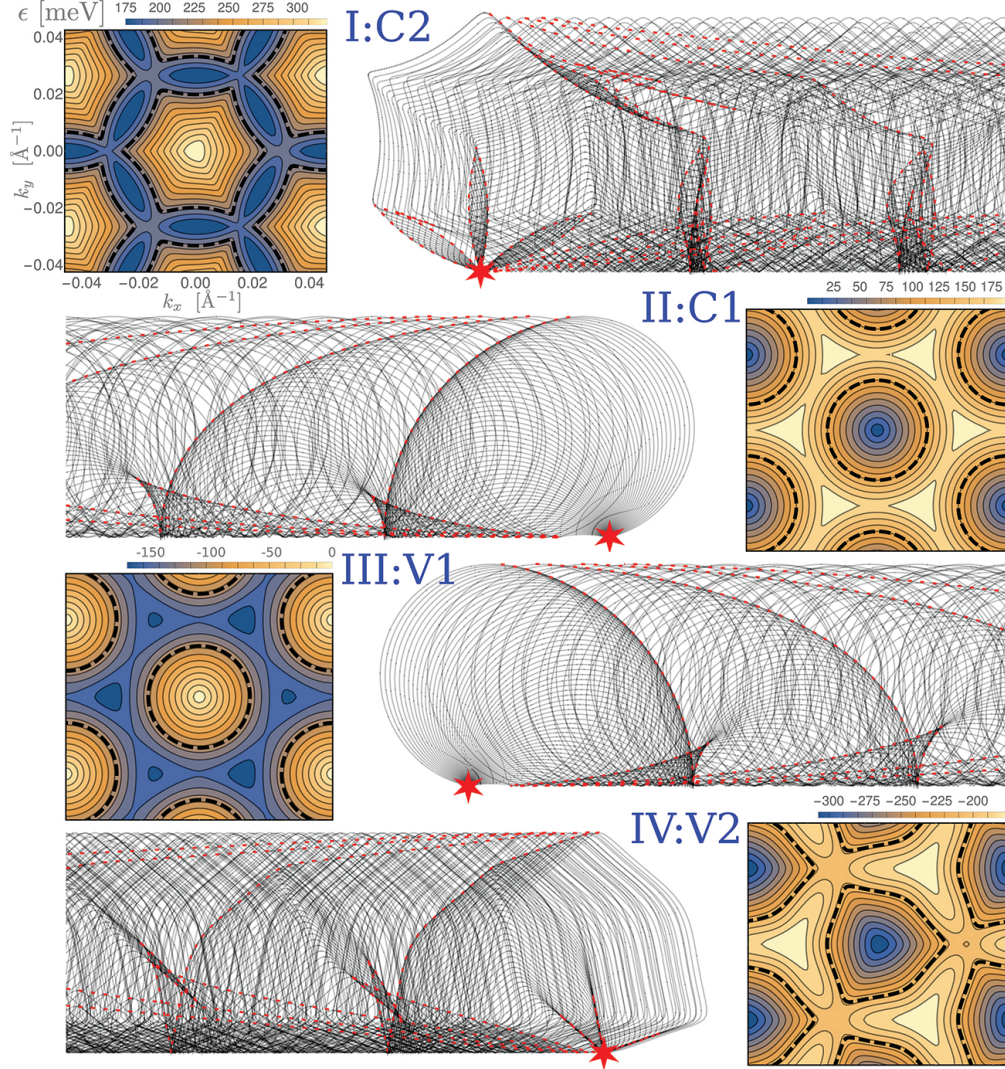
4

Fig. 3. Simulated skipping orbits. Representative ensembles of simulated skipping orbits emanating from an emitter (red star) at the boundary of the graphene/h-BN superlattice possessing the miniband dispersion of Fig. 2A, for selected electron densities I, II, III, and IV marked in Fig. 2B. The corresponding Fermi surfaces are in minibands C2, C1, V1, and V2, respectively, and each one is drawn as a thick, dashed constant-energy contour on the color map of the dispersion. The magnetic field points out of the page, so electron-like carriers turn counter-clockwise and their skipping orbits drift left, and hole-like carriers do the opposite. Red dashed curves mark caustics.

shows the temperature dependence of this effective scattering rate, extracted from the data using the formula $\tau(T)^{-1} = -\frac{2v_F}{\pi L} \log \frac{A_1(T)}{A_1(T_{base})}$. The experimentally observed dependence $\tau(T)^{-1} \propto T^2$ points toward an electron-electron (e-e) scattering mechanism for the suppression of TEF oscillations upon heating, the same mechanism responsible for the evolution of electronic transport from ballistic to the viscous regime [33–35]. Theoretical analysis of spreading of a narrow beam of electrons due to low-angle scattering processes, governed by the Thomas-Fermi-screened e-e interaction, shows
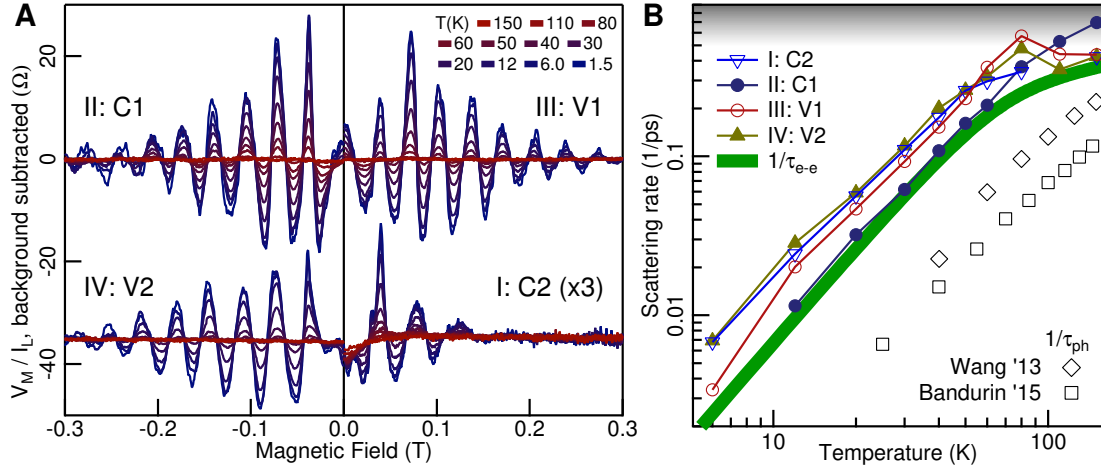
Fig. 4. Temperature dependence of TEF spectra. (**A**) V_M/I_L (B) minus a smooth background [30], for the electron densities I, II, III, and IV marked in Fig. 2B, and temperatures up to 150 K. Increasing the temperature suppresses TEF. (**B**) Circles and triangles: effective scattering rates $\tau(T)^{-1}$ extracted from the amplitude of TEF oscillations in (A). Green heavy curve: theoretical scattering rate τ_{e-e}^{-1} related to the electron-electron interaction. Square and diamond symbols: rate of scattering by phonons τ_{ph}^{-1} inferred from temperature-dependent sheet resistivity reported in [35] and [36]. The detection limit set by noise is shaded.

that for $T \lesssim T_*$ (where $k_B T_* = 2 v_F \sqrt{\frac{k_F}{\pi L}}$), the decay of TEF signal can be described by a scattering rate

$$\tau_{e-e}^{-1} \approx \frac{(k_B T)^2}{2 \hbar v_F k_F} \log\left(\frac{3.6L}{w}\right), \tag{2}$$

where w is the width of the emitting and collecting contacts [30]. Figure 4B shows the theoretical values (calculated without free parameters [30]), of τ_{e-e}^{-1}, including the theoretically predicted crossover to a slower scattering rate for $T > T_*$. The rate of scattering by phonons, τ_{ph}^{-1}, can be inferred from temperature-dependent sheet resistivity of similar encapsulated graphene/h-BN heterostructures of Refs. [35, 36] (Fig. 4B). This inferred τ_{ph}^{-1} is much lower than both experimentally measured $\tau(T)^{-1}$ and calculated τ_{e-e}^{-1}, so it appears that low-angle *e-e* scattering is the dominant mechanism for suppression of TEF.

The direct observation and manipulation of ballistic transport is a powerful probe of the low-energy physics of an electron system. Here, the quasiparticles propagate freely from emitter to collector through ballistic trajectories as long as $\frac{\pi L}{2} = 10\ \mu m$, which is 700 in dimensionless units of the superlattice period. Ballistic motion of ultracold atoms has been seen in homogeneous optical lattices as large as 100 unit cells [37], but in the solid state, the mean free path of electrons in semiconductor 1D superlattices has been limited to 10 unit cells [38]. Our experiment elucidates the key features of miniband electron dynamics in a moiré superlattice, and points toward further explorations of novel transport effects. For instance, the saddle point VHS could host exotic effects caused by enhanced electron-electron interactions [19, 39], and valley-contrasting physics could be accessed by taking advantage of the severe trigonal warping of minibands [40]. For technology, such a clear validation of the miniband conduction properties suggests that graphene/h-BN and perhaps other moiré superlattices may be a practical platform for devices based on miniband

physics. Efficient photocurrent generation at the edge of a graphene superlattice in magnetic field [41] may be caused by the skipping orbits we have observed; furthermore, THz devices such as the Bloch oscillator can benefit from the extremely longer scattering times in this system.

References

[1] L. Esaki, R. Tsu, *IBM Journal of Research and Development* **14**, 61 (1970).

[2] L. Esaki, L. L. Chang, *Physical Review Letters* **33**, 495 (1974).

[3] C. Waschke, *et al.*, *Physical Review Letters* **70**, 3319 (1993).

[4] D. Weiss, K. V. Klitzing, K. Ploog, G. Weimann, *Europhysics Letters (EPL)* **8**, 179 (1989).

[5] H. A. Carmona, *et al.*, *Physical Review Letters* **74**, 3009 (1995).

[6] A. Sandner, *et al.*, *Nano Letters* **15**, 8402 (2016).

[7] C. Albrecht, *et al.*, *Physical Review Letters* **83**, 2234 (1999).

[8] J. Xue, *et al.*, *Nature Materials* **10**, 282 (2011).

[9] R. Decker, *et al.*, *Nano Letters* **11**, 2291 (2011).

[10] C. Ortix, L. Yang, J. van den Brink, *Physical Review B* **86**, 081405 (2012).

[11] M. Kindermann, B. Uchoa, D. L. Miller, *Physical Review B* **86**, 115415 (2012).

[12] J. R. Wallbank, A. A. Patel, M. Mucha-Kruczynski, A. K. Geim, V. I. Fal'ko, *Physical Review B* **87**, 245408 (2013).

[13] M. Yankowitz, *et al.*, *Nature Physics* **8**, 382 (2012).

[14] G. L. Yu, *et al.*, *Nature Physics* **10**, 525 (2014).

[15] Z. Shi, *et al.*, *Nature Physics* **10**, 743 (2014).

[16] L. A. Ponomarenko, *et al.*, *Nature* **497**, 594 (2013).

[17] C. R. Dean, *et al.*, *Nature* **497**, 598 (2013).

[18] B. Hunt, *et al.*, *Science* **340**, 1427 (2013).

[19] W. Yang, *et al.*, *Nano Letters* **16**, 2387 (2016).

[20] D. R. Hofstadter, *Physical Review B* **14** 2239 (1976).

[21] N. Bohr, *Niels Bohr Collected Works* (Elsevier, Amsterdam, 1972), vol. 1, p. 276.

[22] V. S. Tsoi, *Journal of Experimental and Theoretical Physics Letters* **19**, 70 (1974).

[23] C. W. J. Beenakker, H. van Houten, B. J. van Wees, *Europhysics Letters (EPL)* **7**, 359 (1988).

[24] L. Oroszlány, P. Rakyta, A. Kormányos, C. J. Lambert, J. Cserti, *Physical Review B* **77** 081403 (2008).

[25] T. K. Ghosh, A. De Martino, W. Häusler, L. Dell'Anna, R. Egger, *Physical Review B* **77** 081404 (2008).

[26] N. Davies, *et al.*, *Physical Review B* **85**, 155433 (2012).

[27] A. A. Patel, N. Davies, V. Cheianov, V. I. Fal'ko, *Physical Review B* **86**, 081413 (2012).

[28] P. C. van Son, H. van Kempen, P. Wyder, *Physical Review Letters* **58**, 1567 (1987).

[29] T. Taychatanapat, K. Watanabe, T. Taniguchi, P. Jarillo-Herrero, *Nature Physics* **9**, 225 (2013).

[30] See Supplementary Materials.

[31] R. S. Markiewicz, *Journal of Physics: Condensed Matter* **6**, 3059 (1994).

[32] X. Chen, *et al.*, *Physical Review B* **89**, 075401 (2014).

[33] I. Torre, A. Tomadin, A. K. Geim, M. Polini, *Physical Review B* **92**, 165433 (2015).

[34] A. Principi, G. Vignale, M. Carrega, M. Polini, *Physical Review B* **93**, 125410 (2016).

[35] D. A. Bandurin, *et al.*, *Science* **351**, 1055 (2016).

[36] L. Wang, *et al.*, *Science* **342**, 614 (2013).

[37] U. Schneider, *et al.*, *Nature Physics* **8** 213 (2012).

[38] C. Rauch, *et al.*, *Superlattices and Microstructures* **25** 47 (1999).

[39] R. Nandkishore, L. S. Levitov, A. V. Chubukov, *Nature Physics* **8**, 158 (2012).

[40] J. L. Garcia-Pomar, A. Cortijo, M. Nieto-Vesperinas, *Physical Review Letters* **100**, 236801 (2008).

[41] S. Wu, *et al.*, *Science Advances* **2**, e1600002 (2016).

[42] A. Mishchenko, *et al.*, *Nature Nanotechnology* **9**, 808 (2014).

[43] L. Wang, *et al.*, *Science* **350**, 1231 (2016).

[44] M. J. Rooks, *et al.*, *Journal of Vacuum Science & Technology B: Microelectronics and Nanometer Structures* **20**, 2937 (2002).

[45] J. R. Wallbank, M. Mucha-Kruczynski, X. Chen, V. I. Fal'ko, *Annalen der Physik* **527**, 25 (2014).

[46] G. X. Ni, *et al.*, *Nature materials* **14**, 1217 (2015).

[47] H. van Houten, *et al.*, *Physical Review B* **39**, 8556 (1989).

[48] B. J. van Wees, *et al.*, *Physical Review Letters* **60**, 848 (1988).

[49] A. M. DaSilva, *et al.*, *Physical Review B* **91**, 245422 (2015).

[50] Q. Li, S. Das Sarma, *Physical Review B* **87**, 085406 (2013).

[51] G. F. Giuliani, J. J. Quinn, *Physical Review B* **26**, 4421 (1982).

[52] A. A. Abrikosov, *Fundamentals of the Theory of Metals* (Elsevier Science Publishing, 1988).

[53] R. N. Gurzhi, A. N. Kalinenko, A. I. Kopeliovich, *Physical Review B* **52**, 4744 (1995).

Materials and Methods

All measurements were performed in the helium vapor space of a flow cryostat with a superconducting magnet. Transverse electron focusing (TEF) spectra were measured by a lock-in amplifier, sourcing a small 263 Hz, 50 nA rms alternating current into the emitter contact, which ensured that the voltage drop at the contact was less than $k_B T/e$.

Sample Fabrication

The two-dimensional system we investigated was a heterostructure of monolayer graphene encapsulated in hexagonal boron nitride (h-BN), with a bilayer graphene back gate. Flakes of monolayer and bilayer graphene (from highly oriented pyrolytic graphite, Momentive Performance Materials ZYA grade) and of h-BN (from single crystals synthesized at high pressure and high temperature) were exfoliated mechanically using tape (3M Scotch), deposited on oxidized (90 nm oxide) silicon (WRS Materials) substrates, and identified by inspection of optical microscope images. The flakes of h-BN had thicknesses ≈ 30 nm. The heterostructure was assembled by a top-down pick-up technique using a temperature-sensitive adhesive film of polypropylene carbonate (Sigma-Aldrich) mounted on a clear backing of Polydimethylsiloxane (Dow Corning Sylgard 184), as described in [36]. The assembled heterostructure was deposited on a chip of oxidized (300 nm oxide), degenerately doped silicon. We did not intentionally orient the flakes or anneal the final heterostructure to align the crystal axes as other authors have done [42, 43]. The heterostructure had no h-BN step edges or segregated bubbles over or under the device area. All patterns were defined by electron-beam lithography, using beams of 10 or 30 keV energy to expose the resist PMMA 950 A4 or A5 (MicroChem). The exposed pattern was developed by a chilled 1:3 mixture of water and isopropanol, in order to avoid swelling the resist which can lead to cracking or delamination from the h-BN surface [44]. The device geometry, which includes three narrow local contacts along a linear boundary for carrier reflections, was defined by direct reactive ion etching in a 150 mTorr plasma of CHF_3/O_2 with flow rates 50 and 5 sccm, respectively. The local contacts were etched to a nominal width of $w = 250$ nm, and adjacent pairs were separated by lengths 2.5 and $L = 6.3\,\mu$m. Ohmic contacts to the device as well as contact to the bilayer back gate were formed by electron-beam evaporation of Cr/Au electrodes onto the edge of graphene exposed by the etch, as in [36].

Supplementary Text

Size of the moiré unit cell

Figure S1 shows the quantity $(V_M - V_L)/I_R$ measured as a function of V_g at $B = 0$. The grounded absorbers that drain the injected current are placed to the left side of the device (Fig. 1A). We inject current into the right-most local contact R rather than L. Whenever the sample's 2D sheet resistivity is high, such as when V_g is placed at or near either the Dirac point (DP) or the secondary Dirac points (SDPs), transport is diffusive and there will be an appreciable voltage drop $(V_M - V_L)$ owing to the relative positions of the middle (M) and left (L) contacts along the current flow from right to left. Hence the quantity $(V_M - V_L)/I_R$ may be considered a quasi-local resistance of the device that indicates the sheet resistivity of the sample. As expected and previously observed [16–18], we find the resistivity peaks corresponding to the DP and the SDPs, with the SDP peak in the conduction

band significantly smaller than the others. The gate voltage difference between DP and SDP in the valence band is 2.92 V.

In higher magnetic fields, Landau quantization is apparent, which provides an absolute calibration of the geometric gate capacitance: $C_g = 0.131\ \mu\text{F/cm}^2$ (equal to the parallel-plate capacitance of dielectric thickness 27 nm and permittivity 4). The number of electronic states that fills one miniband, i.e. the number of states between the DP and the SDP, is given by $n_0 = 2\sqrt{3}(b/2\pi)^2$. The moiré wave vector length b can be inferred from the relation (taking proper account of the quantum capacitance) $\Delta V_g = \Delta E_F/e + en_0/C_g$ where $\Delta E_F \approx vb/2$ is the Fermi level difference between DP and SDP. The solution is $b = 0.051\ \text{Å}^{-1}$, which corresponds to a 14 nm moiré period.

Model of miniband structure

We calculate the superlattice minibands of a fully aligned (misalignment angle $\theta = 0$) graphene/h-BN heterostructure by numerically diagonalizing the Hamiltonian [12, 45],

$$\hat{H} = v\vec{p} \cdot \vec{\sigma} + (U_0^+ f_+ + U_0^- f_-) + \xi\sigma_3 \left(U_3^+ f_- + U_3^- f_+ \right) + \frac{\xi\vec{\sigma}}{b} \cdot \left[\vec{l}_z \times \nabla \left(U_1^+ f_- + u_1^- f_+ \right) \right]. \qquad \text{(S.1)}$$

Here σ_i are Pauli matrices, acting on Bloch states $(\phi_{AK}, \phi_{BK})^T$ in the K valley ($\xi = 1$) and $(\phi_{BK'}, -\phi_{AK'})^T$ in the K' valley ($\xi = -1$), and $\hbar = 1$. Functions $f_\pm = \sum_m (\pm 1)^{m+\frac{1}{2}} e^{i\vec{b}_m \cdot \vec{r}}$ are written using the six shortest Bragg vectors of the moiré superlattice, $\vec{b}_{m=0,\cdots,5} = R_{m\pi/3}(0, b)$, where R_φ describes anticlockwise rotation by angle φ, and we use $b = 0.053\ \text{Å}^{-1}$ for the fully aligned heterostructure. The first term in $\hat{H}$ is the Dirac Hamiltonian of unperturbed graphene, while the remaining terms describe the superlattice perturbation. Among these, the first term describes a simple potential modulation; the second a A-B sublattice asymmetry, locally imposed by the substrate; and the third a modulation of A-B hopping. The strength of each of these terms is characterized using parameters $U_{i=0,1,3}^\pm$, where $+/-$ is used for the part of each term which is symmetric/antisymmetric under the in-plane spatial inversion symmetry.

In principle, each parameter $U_i^\pm$ takes an arbitrary value. However, two microscopic models, one based on the hopping between the graphene and h-BN lattices [11], and the other on scattering of graphene electrons off quadrupole electric moments in the h-BN layer [12], predict

$$\{U_{i=0,1,3}^\pm\} = \epsilon^\pm \left\{ \frac{\pm 1}{2}, -1, \frac{-\sqrt{3}}{2} \right\}. \qquad \text{(S.2)}$$

By using Eq. (S.2) we reduce the number of parameters used to describe the superlattice perturbation from six in Eq. (S.1) to two: (ϵ^+, ϵ^-). We treat them as variable parameters, and establish their values with a fitting procedure using the experimentally measured TEF oscillation. First we note that the gate voltages $\{V_v^1, V_c^1, V_v^2, V_c^2\}$ at which TEF oscillations terminate (highlighted in Fig. 2B), correspond to saddle points in the miniband structure. Then, we compute the miniband structure resulting from each choice of (ϵ^+, ϵ^-), and compare its prediction for the gate voltage ratios $\frac{V_v^1 - V_v^2}{V_c^1 - V_v^1}$ and $\frac{V_c^2 - V_c^1}{V_c^1 - V_v^1}$ against the experimentally observed values. To calculate these gate voltage ratios from the Fermi energy E_F, we take proper account of the geometric gate and quantum capacitances using the relation $V_g = E_F/e + en(E_F)/C_g$, where e is the electron charge, $n(E_F)$ is the electron density, and $C_g = 0.131\ \mu\text{F/cm}^2 = 4e \cdot (\text{moiré unit cell area})^{-1} \cdot (2.75\ \text{V})^{-1}$ is the measured geometric

capacitance. Figures S2A and B show the predicted gate voltage ratios $\frac{V_v^1-V_v^2}{V_c^1-V_v^1}$ and $\frac{V_c^2-V_c^1}{V_c^1-V_v^1}$ as a function of ϵ^+ and ϵ^-. We note that it is sufficient to consider only positive values of $\epsilon^\pm$ as the miniband structure is invariant under (i) $\epsilon^- \to -\epsilon^-$ and (ii) $(\epsilon^+, \epsilon^-) \to R(2\pi/3)(\epsilon^+, \epsilon^-)$ [45]. Quantitative comparison to values measured in experiment constrains (ϵ^+, ϵ^-) as shown in the form of confidence regions depicted in Figs. S2C and D. We visually estimate a standard error of $\Delta V_g = 0.03$ V in determining the gate voltage positions of a saddle point. The 1σ confidence region lies within $\epsilon^+ \approx 0.05 \cdot vb = 17$ meV and $|\epsilon^-| < 0.01 \cdot vb = 3$ meV, and the match is best for $\epsilon^- \approx 0$ meV. Hence we choose $(\epsilon^+, \epsilon^-) = (17 \text{ meV}, 0 \text{ meV})$ to calculate the miniband structure, electron dynamics, and TEF spectra shown in all figures in the main text.

Previous optical studies of graphene/h-BN heterostructures [15, 46] also employed model (S.2) for the superlattice perturbation, but assumed $\epsilon^- = 0$ *a priori*. Here, we have provided experimental justification for asserting $\epsilon^- = 0$ within this model, and provided a fit of $\epsilon^+ = 17$ meV, which is comparable to previously estimated values [15, 46].

Semiclassical model of TEF spectra

We model the device shown in Fig. 1A as a wide graphene/h-BN strip with an emitter and two collectors placed along the lower boundary. We choose to orient the boundary along the x-axis, which coincides with a direct lattice vector of moiré pattern, but find that the main features in the TEF spectra are insensitive to this choice (Fig. S3 below and corresponding text). To mimic the important features in the measured non-local resistance, $(V_M - V_R)/I_L$, especially the voltage-magnetic field dependence of the caustic focusing peaks, we populate forward propagating states at the emitter with N_L electrons according to their density of states, and model their evolution using the semiclassical equation of motion (Eq. 1 of the main text) and specular reflection at the sample boundary. In Fig. 2C and Fig. S3, we plot $(N_M - N_R)/N_L$, where N_M is the number of electrons that impinge on contact M during their semiclassical motion (taking the nominal contact width $w = 250$ nm), and N_R is a smooth background, calculated as $N_R = \sum_{i=1}^{N_L} w/d_i$, with d_i the distance between consecutive skips along the boundary for the ith trajectory.

An estimate of the magnitude of oscillations in the non-local resistance $(V_M - V_R)/I_L$ can be obtained if the calculated ratio $(N_M - N_R)/N_L$ is treated as an estimate of the ratio of currents $(I_M - I_R)/I_L$ and then multiplied by the resistance, R, of the point contacts ($I_{i=L,M,R}$ is the current passing through contact i) [47]. For our measurement set up it is not possible to measure the point contact resistance separately from that of the graphene-metal contacts for the leads. However, a rough estimate may be obtained using the formula for classical ballistic point contacts, $R = \frac{h}{4e^2} \frac{\pi}{wk_F}$ [48], where the factor 4 is graphene's four-fold spin-valley degeneracy. For $V_g = 1.5$ (corresponding to $k_F = 0.022 \text{ Å}^{-1}$) this gives $R \approx 360 \, \Omega$ so that the calculated oscillations of 0.2 in $(N_M - N_R)/N_L$ (Fig. S3) translate into oscillations in the non-local resistance of $\approx 70 \, \Omega$, which can be compared to the measured oscillations of about $30 \, \Omega$ for this gate voltage. The difference between the measured and calculated results may be due to possible differences in the true width of the contacts compared to their nominal width w (including possible edge roughness and electrostatic potentials), a lack of knowledge of the true angular acceptance and emittance of the contacts, or scattering of electrons from their ballistic trajectories.

Background subtraction for TEF spectra

The procedure for extracting a smooth background for spectra in Fig. 4A is the binomial smoothing filter, a.k.a. a Gaussian filter. We applied a Gaussian filter function with a full width at half maximum of 50 mT, which exceeds the periodicity of the TEF oscillations. This width is sufficient to ensure that the oscillation amplitudes are not significantly affected by the subtraction, which is readily checked by varying the chosen width.

More examples of calculated TEF spectra

The left panels of Fig. S3 display further examples of miniband structures, calculated using Hamiltonian ((S.1)) and several different choices of the superlattice parameters $U_i^\pm$. The remaining panels display the corresponding TEF spectra calculated for several choices of the angle ϕ (measured between moiré Bragg vector $\vec{b}_0$ and the direction perpendicular to the device edge). Importantly, the comparison of panels for various ϕ shows that the main features of the TEF spectra are independent of angle ϕ (the spectra will repeat after $\phi = 60°$). In particular, the gate voltages $\{V_v^1, V_c^1, V_v^2, V_c^2\}$ at which the TEF oscillations in a given miniband terminate, are set by the energy of saddle points in the minibands, and do not depend on ϕ.

Influence of electron-electron scattering on the temperature dependence of the visibility of the TEF oscillations

To model the temperature dependent decay of the TEF oscillations, we calculate the spread of a bunch of non-equilibrium electrons as they propagate from the collector to the emitter using a Boltzmann transport equation. We take an initial electron distribution, injected at time $t = 0$, with wavevectors concentrated in a small range of angles, to mimic the focused electrons near the caustic trajectory. After this, the role of the magnetic field is non-essential to our model, as we shall consider the spread of the electron distribution in the direction transverse to the cyclotron path (below described by coordinate y), while the overall propagation of its center of mass displaces along the segment of a cyclotron semicircle to $x = vt$. Also, we neglect the moiré perturbation, which formally limits this calculation to Fermi energies within about half the band width of the first miniband (densities corresponding to C1 and V1 in the measurements).

Then, the Boltzmann transport equation with electron-electron collisions reads [51, 52],

$$\left[\partial_t + v\sin(\theta_1)\partial_y\right] f(\vec{k}_1) = I\{f(\vec{k}_1)\}, \tag{S.3}$$

$$I\{f(\vec{k}_1)\} = \frac{8\pi|W|^2}{(2\pi)^4 v} \int d\vec{k}_2 d\vec{k}_3 \delta(k_1 + k_2 - k_3 - k_4) g_{1,3} g_{2,4} F,$$

$$F = \left[-f(\vec{k}_1)f(\vec{k}_2)(1 - f(\vec{k}_3))(1 - f(\vec{k}_4)) + f(\vec{k}_3)f(\vec{k}_4)(1 - f(\vec{k}_1))(1 - f(\vec{k}_2))\right].$$

Here $\theta_i = \arctan(k_i^y/k_i^x)$, $\vec{k}_i = (k_i^x, k_i^y)$, the distribution function $f(\vec{k}_1)$ depends implicitly on y, $\vec{k}_4 = \vec{k}_1 + \vec{k}_2 - \vec{k}_3$ is determined by momentum conservation, $k_i = |\vec{k}_i|$, $g_{i,j=1,\cdots 4} = \frac{1+\cos(\theta_i - \theta_j)}{2}$ are the chirality factors [50], k_F is the Fermi wavevector, and we have taken into account spin-valley degeneracy. For the collision integral, $I\{f(\vec{k}_1)\}$, we use a contact potential $V(\vec{r}_1 - \vec{r}_2) = W\delta(\vec{r}_1 - \vec{r}_2)$ and $W = \frac{\pi v}{2k_F}$, which is equivalent to the RPA screened Coulomb interaction, $v_q/(1 + v_q\Pi(q, \omega))$,

[50] (where $v_q = 2\pi e^2/(\kappa q)$, κ is the background dielectric constant, and $\Pi(q, \omega)$ is the irreducible polarizability) in the limit $v_q \Pi(q, \omega) \approx v_q \Pi(q, 0) = \frac{4e^2 k_F}{\kappa v q} \gg 1$.

To evaluate $I\{f(\vec{k}_1)\}$ in Eq. (S.3) we approximate,

$$f(\vec{k}_i) \approx \frac{1}{\exp[\frac{v\Delta k_i}{k_b T}] + 1} + \frac{\delta\mu(\theta_i)}{2k_B T} \frac{1}{1 + \cosh(\frac{v\Delta k_i}{k_B T})} \tag{S.4}$$

where $\Delta k_i = k_F - k_i$, the Boltzmann constant is k_B, and $\delta\mu(\theta_i) \ll k_B T$ is a small, angle dependent, shift in the chemical potential attributed to electrons with momenta orientated along θ_i.

For this distribution $I\{f(\vec{k}_1)\}$ is sharply peaked when $\Delta k_i/k_F \lesssim k_B T/(vk_F) \ll 1$ for each $i = 1, \cdots 4$. Also, by momentum conservation,

$$\Delta k_4 \approx k_F \left(\sqrt{3 + 2\cos(\theta_2 - \theta_1) - 2\cos(\theta_3 - \theta_1) - 2\cos(\theta_3 - \theta_2)} - 1 \right),$$

so that possible choices of θ_2 and θ_3 which satisfy $\Delta k_4/k_F \ll 1$ are divided into the three cases displayed in Fig. S4: either (i) $\theta_2 = \theta_1 + \pi + \Delta\theta_2$, or (ii) $\theta_3 = \theta_1 + \Delta\theta_3$, or (iii) $\theta_2 = \theta_3 + \Delta\theta_2$, where $\Delta\theta_i \lesssim k_B T/vk_F$. For process (i) the initial pair of electrons can scatter into any state near the Fermi line, where as for cases (ii) and (iii) the angle of the scattered electron only deviates from that of an initial state by an amount $\lesssim k_B T/vk_F$. Because of this the contributions of processes (ii) and (iii) towards the relaxation rates for electron distributions are $\sim (mk_B T/vk_F)^2$ times lower than that generated by process (i) [53], which will be studied below (m is the index of the angular harmonic).

By concentrating on process (i), our focused non-equilibrium electron distribution will typically decay by producing a beam of holes propagating in the opposite direction. As the holes separate quickly from the electron bunch, their effect on the decay of the electron distribution can be neglected. Hence we use $\delta\mu(\theta_2) = \delta\mu(\theta_4) = 0$ which reduces Eq. (S.3) to,

$$\left[\partial_t + v\sin(\theta_1)\partial_y\right] \delta\mu(\theta_1) = \frac{|W|^2}{32k_B T\pi^3} \int dk_1 d\vec{k}_2 d\vec{k}_3 \delta(k_3 - k_1 + k_4 - k_2) g_{1,3} g_{2,4} \frac{\delta\mu(\theta_3) - \delta\mu(\theta_1)}{\prod_{i=1,\cdots 4} \cosh(\frac{v\Delta k_i}{2k_B T})}.$$

Next, we expand $\delta\mu(\theta)$ in terms of its angular harmonics, $f(m)$,

$$\delta\mu(\theta) = \sum_m e^{im\theta} f(m),$$

so that the transport equation becomes,

$$\partial_t f(m) + \frac{v}{2i}\partial_y(f(m-1) - f(m+1)) = -\frac{f(m)}{\tau_m}. \tag{S.5}$$

Here we have introduced the relaxation time for the mth harmonic,

$$\frac{1}{\tau_m} = \frac{-|W|^2}{32\pi^3 k_B T} \int dk_1 dk_2 dk_3 d\tilde{\theta}_2 d\tilde{\theta}_3 \, k_2 k_3 \, \delta(k_1 + k_2 - k_3 - k_4) g_{1,3} g_{2,4} \frac{e^{im\tilde{\theta}_3} - 1}{\prod_{i=1,\cdots 4} \cosh(\frac{v\Delta k_i}{2k_B T})} \tag{S.6}$$

and defined $\tilde{\theta}_3 = \theta_3 - \theta_1$, and $\tilde{\theta}_2 = \theta_2 - \theta_1$.

For process (i), $\tilde{\theta}_2 = \pi + \Delta\theta_2$ and the energy conserving delta function can be expressed as,

$$\delta(k_1 + k_2 - k_3 - k_4) = \frac{1}{k_F |\sin(\tilde{\theta}_3)|} \delta(\frac{\Delta k_1 + \Delta k_2 - 2\Delta k_3 - (\Delta k_2 - \Delta k_1)\cos(\tilde{\theta}_3)}{k_F \sin(\tilde{\theta}_3)} - \Delta\theta_2),$$

13

which simplifies the integration over $\tilde{\theta}_2$ and leads to,

$$\frac{1}{\tau_m} = \frac{(k_B T)^2}{v k_F} I(m), \tag{S.7}$$

$$I(m) \equiv \frac{1}{512\pi} \int d\xi_1 d\xi_2 d\xi_3 \, d\tilde{\theta}_3 \frac{\left[1 + \cos(\tilde{\theta}_3)\right]^2 \left[\cos(m\tilde{\theta}_3) - 1\right]}{|\sin(\tilde{\theta}_3)| \cosh(\frac{\xi_1 + \xi_2 - \xi_3}{2}) \prod_{i=1,\cdots 3} \cosh(\frac{\xi_i}{2})}$$

$$\approx \begin{cases} \alpha \log(\beta|m| + \gamma), & m \neq 0 \\ 0, & m = 0 \end{cases}$$

where $\alpha \approx 0.518$, $\beta \approx 2.28$, and $\gamma \approx -0.675$.

The collision integral increases with m, so that the spreading of a narrow beam of electrons is dominated by the relaxation of harmonics with $m \gg 1$. Hence, we treat m as a continuous variable (and correspondingly allow θ to range between $\pm\infty$), and approximate $f(m-1) - f(m+1) \approx -2\partial_m$ in Eq. (S.5) to arrive at,

$$\partial_t f(t, y, m) - \frac{v}{i} \partial_y \partial_m f(t, y, m) = -\frac{1}{\tau_m} f(t, y, m),$$

where we explicitly list the transverse coordinate and time dependences in the distribution function. By taking the Fourier transform in the y-direction, $\hat{f}(t, q_y, m) = \frac{1}{2\pi} \int dy f(t, y, m) e^{-iq_y y}$, we obtain,

$$\partial_t \hat{f}(t, q_y, m) - v q_y \partial_m \hat{f}(t, q_y, m) = -\frac{1}{\tau_m} \hat{f}(t, q_y, m),$$

which is solved using

$$\hat{f}(t, q_y, m) = \hat{f}_0(q_y, m + v q_y t) e^{-\frac{G(m + v q_y t) - G(m)}{v q_y}}, \qquad \frac{dG(m)}{dm} = \frac{1}{\tau_m},$$

where $\hat{f}_0(q_y, m) = \hat{f}(t = 0, q_y, m)$. For simplicity, we assume the beam to be initially Gaussian in y, with characteristic width a_e (the width of the emitter) and fully collimated, so that $\hat{f}_0(q_y, m) = (2\pi)^{-2} e^{-\frac{q_y^2 a_e^2}{2}}$, and,

$$f(t, y, \theta) = \frac{1}{(2\pi)^2} \int dq_y dm \, e^{-\frac{q_y^2 a_e^2}{2}} e^{-\frac{G(m + v q_y t) - G(m)}{v q_y}} e^{iq_y y} e^{im\theta},$$

models the result of the transverse spreading of the beam after the time $t = \frac{\pi L}{2v}$ needed for it to reached the collecting electrode. To model the temperature dependent signal at the collector, $R(T)$, we take the convolution of the total distribution of electrons, $\int f(\frac{\pi L}{2v}, y, \theta) d\theta$, with a Gaussian weigh factor, $\exp(-y^2/2a_c^2)$, mimicking the collector width a_c, so that,

$$\frac{R(T)}{R(0)} = \frac{A}{\sqrt{2\pi}} \int dq_y \, e^{-\frac{q_y^2 A^2}{2}} e^{-\frac{G(q_y \pi L/2) - G(0)}{v q_y}}, \tag{S.8}$$

$$= \frac{\sqrt{2}A}{\sqrt{\pi}} \int_{\frac{2(1-\gamma)}{\pi \beta L}}^{\infty} dq_y e^{-\frac{q_y^2 A^2}{2}} e^{-\frac{\alpha(k_B T)^2}{v^2 k_F} \left[(\frac{\pi L}{2} + \frac{\gamma}{\beta q_y}) \log(\frac{\beta q_y \pi L}{2} + \gamma) - \frac{\pi L}{2} + \frac{1-\gamma}{\beta q_y} \right]},$$

$$A^2 = a_c^2 + a_e^2,$$

14

where lower cut off of $\frac{2(1-\gamma)}{\pi\beta L}$ for the integral is introduced to exclude unphysical harmonics with $m < 1$.

In Fig. S5 we display the factors in the integrand of Eq. (S.8) for various temperatures. When $T \lesssim T_*$, where

$$T_* = \sqrt{\frac{2v^2 k_F}{\alpha \pi L k_B^2}},$$

the integral is dominated by the wide tails of the integrand, extending up to $q_y \lesssim A^{-1}$, where it decays exponentially with L and T^2 (here $T_* \approx 45\,\mathrm{K}$). Hence for $T \lesssim T_*$, the decay of the TEF signal can be described using a scattering time, $\tau_{\text{e-e}}$, which we define similarly to that used for the experimental data in the main text,

$$\tau_{\text{e-e}}^{-1} \equiv -\frac{2v}{\pi L} \log\left(\frac{R(T)}{R(0)}\right) \approx \frac{\alpha(k_B T)^2}{v k_F} \log\left(\frac{\beta \pi L}{2A}\right). \tag{S.9}$$

Note that, this scattering rate is slower than the quasiparticle life-time calculated in Ref. [50].

For temperatures $T > T_*$, the tail of the integrand in Eq. (S.8) for large q_y becomes suppressed, and the whole integral for $R(T)$ converges to a quantity whose dependence on L and hence t follows a power law rather than an exponential as a function of time. This crossover of the signal decay with time leads to a slower decrease of $R(T)/R(0)$ with increasing temperature above T_*.

In Fig. S6 the numerically evaluated form of $\tau_{\text{e-e}}^{-1}$ (solid green line) is compared to the approximate asymptotic behavior set by Eq. (S.9) (dashed green line), and the scattering rates extracted from either the measured TEF peak heights or TEF peak areas using the recipe described in the main text. For the calculated scattering rate, we use $A = \frac{w}{\sqrt{12}}$ to model the decay of the peak heights (Fig. S6A), where $w = 0.25\,\mu\mathrm{m}$ is the width of the collector, and the $\sqrt{12}$ factor comes from matching the variance of the Gaussian distribution to that of a rectangular distribution. For Fig. S6B we take $A = \frac{L/2}{\sqrt{12}}$ because integrating the TEF signal to obtain the area of the peak, whose width is approximately half of the TEF periodicity, is approximately equivalent to using a collector with width $L/2$. In both cases the calculated and measured scattering rates are comparable, and the dependence of the calculated scattering rate on A is weak (logarithmic).
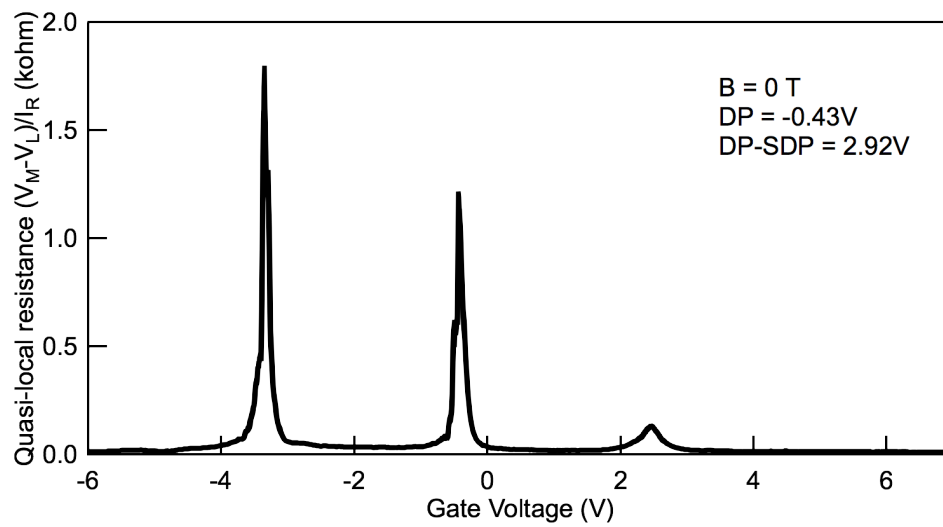
15

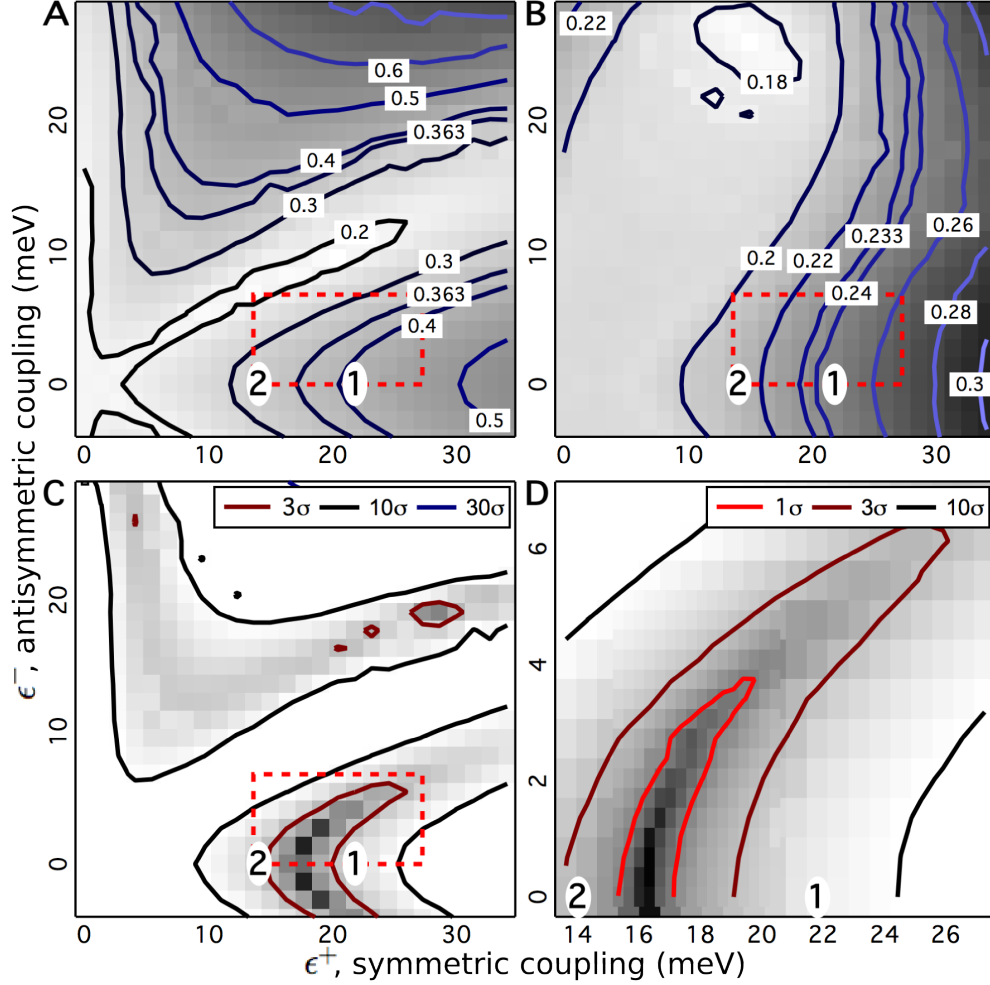**Fig. S1.** The quasi-local resistance $(V_M - V_L)/I_R$ as a function of V_g, at $B = 0$.

Fig. S2. (**A**) The prediction for the gate voltage ratio $\frac{V_v^1 - V_v^2}{V_c^1 - V_v^1}$ as a function of moiré perturbation parameters ϵ^+ and ϵ^-. The value observed in experiment is 0.363. "1" marks parameters used in [12], and "2" denotes parameters in [46]. (**B**) Same as (A) for $\frac{V_c^2 - V_c^1}{V_c^1 - V_v^1}$. The observed value is 0.233. (**C**) Confidence regions for the estimation of parameters (ϵ^+, ϵ^-), obtained by matching the calculated values in (A) and (B) with the experimentally observed values. Dark color is more likely as the prediction is more similar to experiment; contours are boundaries of confidence regions. (**D**) Zoom into the red dashed box in (A)-(C). The best choice of parameters is $(\epsilon^+, \epsilon^-) = (17\,\mathrm{meV}, 0\,\mathrm{meV})$.
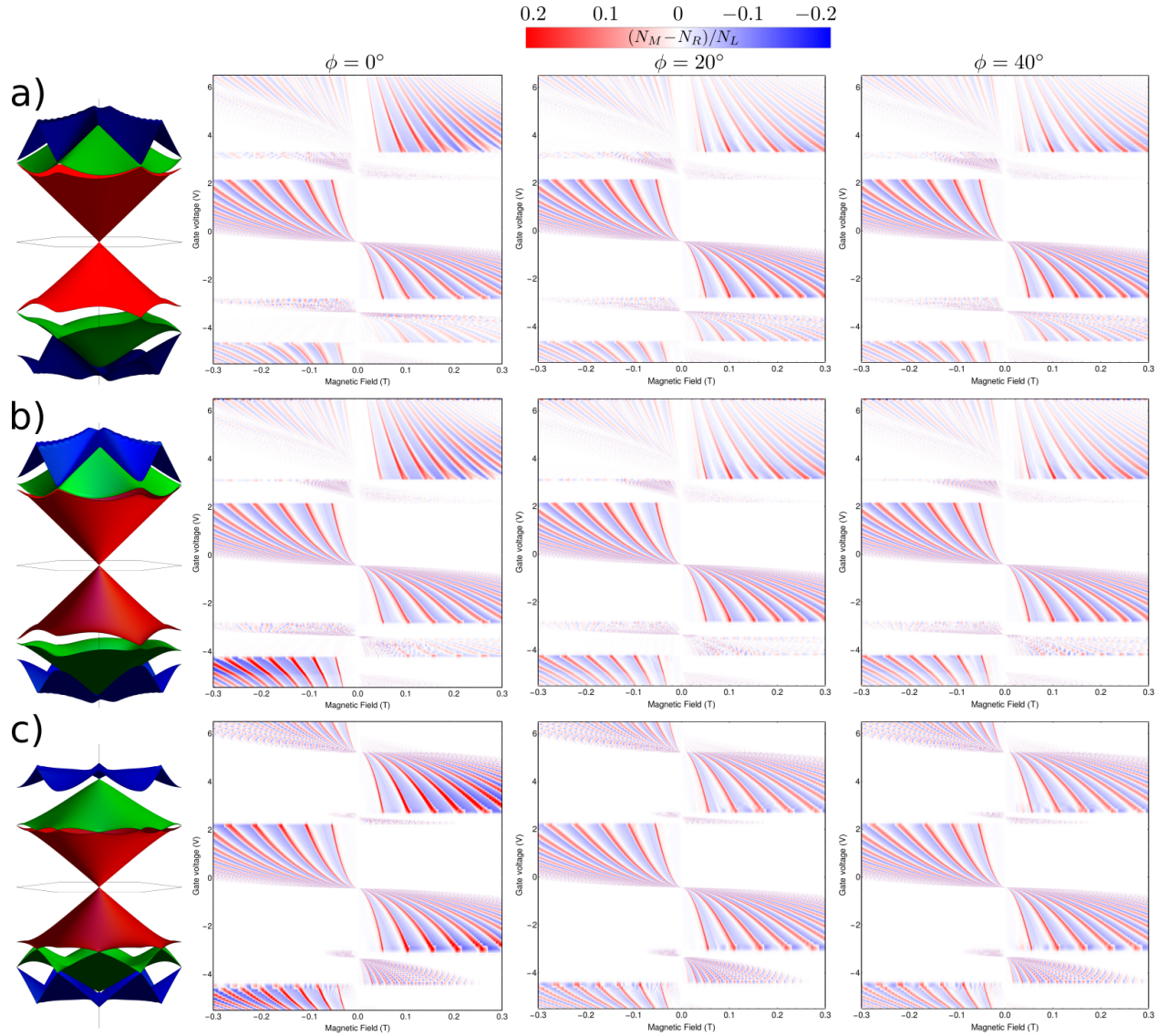
17

Fig. S3. The miniband structures and corresponding TEF spectra calculated for $\phi = 0°$, $20°$, and $40°$. The superlattice parameters are chosen as either (**A**) $\epsilon^+ = 17\,\text{meV}$, $\epsilon^- = 0$, in accordance with the main text, (**B**) $U^+_{i=0,1,3} = \{-8.4, -10.7, -8.3\}\,\text{meV}$, $U^-_{i=0,1,3} = \{-5.6, 3.9, 3.4\}\,\text{meV}$ in accordance with Ref. [49] (a translation of the superlattice [45] was employed to emphasize the inversion symmetric part of the perturbation), or (**C**) $U^+_{i=0,1,3} = \{-52, 0, 0\}\,\text{meV}$, $U^-_{i=0,1,3} = \{0, 0, 0\}$, representing a scalar potential perturbation.
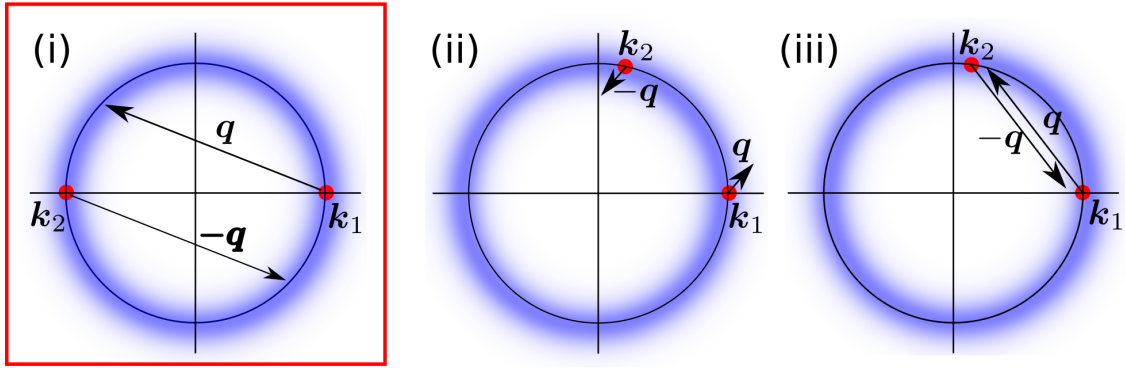
Fig. S4. The three possible ways for initial electron states (red) with wavevectors $\vec{k}_1$ and $\vec{k}_2$ ($\vec{q} = \vec{k}_3 - \vec{k}_1$) to scatter while conserving energy and momentum, and for which all initial and final states lie close to the Fermi line (blue). Only the process (i) can scatter the initial electron states through arbitrary angles.
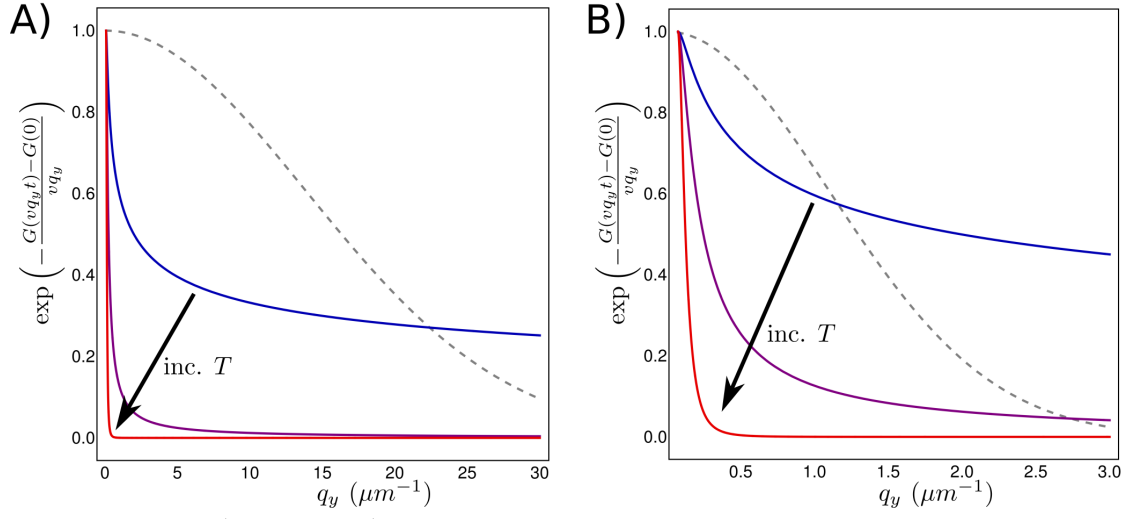
Fig. S5. Plots of $\exp\left(-\frac{G(vq_yt)-G(0)}{vq_y}\right)$ for $T = 0.5T_*$ (blue), $T = T_*$ (purple), and $T = 2T_*$ (red). Relaxation rates are taken from Eq. (S.7), $t = \pi L/(2v)$ and $L = 6.3\,\mu$m. The grey dashed line displays $\exp\left(\frac{-k^2A^2}{2}\right)$ for (**A**) $A = w/\sqrt{12}$ where $w = 0.25\,\mu$m and (**B**) $A = L/(2\sqrt{12})$.
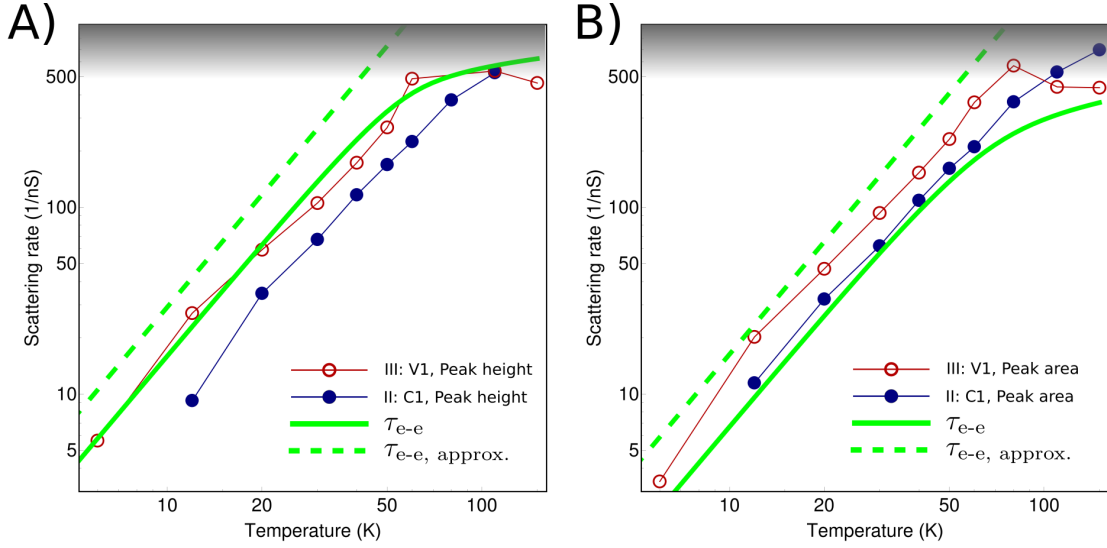
Fig. S6. (**A**) The effective scattering rates, either extracted from the heights of the measured TEF peaks for the densities in bands C1 and V1 (red and blue circles) used in Fig. 4 of the main text, or, calculated using either the numerically evaluated form of $\tau_{\text{e-e}}^{-1}$ (solid line) or its asymptotic Eq. (S.9) (dashed line) using $A = w/\sqrt{12}$ where $w = 0.25\,\mu$m. Note that the Fermi wavevector is almost identical for these two densities. (**B**) The same as (A) except extracting the scattering rates from the measured TEF peak areas, and calculating them using $A = L/(2\sqrt{12})$. Shading is used to show the area for which the measured signal TEF has decayed too much for the scattering rate to be reliably extracted.